Engenharia Agrícola

ISSN: 1809-4430 (on-line)

www.engenhariaagricola.org.br

Scientific Paper

Doi: http://dx.doi.org/10.1590/1809-4430-Eng.Agric.v42n2e20210184/2022

CROP CLASSIFICATION BASED ON A GAOFEN 1/WIDE-FIELD-VIEW TIME SERIES

Yinjiang Jia[1], Xiaoyu Zhang[1], Huaijing Zhang[1], Zhongbin Su[1*]

[1*]Corresponding author. Northeast Agricultural University/ Harbin, China.
E-mail: suzb001@163.com | ORCID ID: https://orcid.org/0000-0002-8966-8933

KEYWORDS

crop classification, vegetation index, time series, support vector machines, adaptive mutation particle swarm optimization.

ABSTRACT

The accurate acquisition of crop planting area information allows for agricultural management departments to understand crop production information promptly. Concurrently, support vector machine (SVM) algorithms are unable to determine parameter combinations in remote sensing image crop classification to obtain optimal classification results. To solve this issue, this paper proposes an SVM that is optimized by the adaptive mutation particle swarm optimization algorithm. To test the algorithm, we undertook an experiment in Acheng District, Harbin City, Heilongjiang province, China, using Gaofen 1/wide-field-view satellite images to construct a time series for various vegetation indices. The SVM model with optimized parameters was compared with a traditional backpropagation neural network, a decision tree, and an SVM without parameter optimization. The experimental results verified that the improved SVM model obtained the highest classification accuracy.

INTRODUCTION

A timely and accurate understanding of crop planting structure provides a basis for agricultural situation monitoring and yield estimation and has important practical significance for guiding agricultural production, formulating agricultural policies, and adjusting agricultural planting structure (Chang-an et al., 2019; Yinjiang et al., 2020). Traditional crop classification methods primarily use visual interpretation, which relies heavily on expert knowledge and may encounter various problems, such as a high level of subjectivity, poor timelines, and low operational efficiency (Silva et al., 2013; Qian et al., 2017; Han & Meng, 2019). Remote sensing technology provides a technical means for the rapid extraction of crop planting structures in large areas. Satellite remote sensing, which is widely used in crop classification, has particularly unique advantages, including being able to provide image data with different temporal, spatial, and spectral resolutions (Caiyun & Zhixiao, 2012; Qing-bo Zhou et al., 2017).

Vegetation indices use a combination of satellite band data and can effectively reflect the spectral characteristics of plants during different growth periods. However, as the same crops may be planted in different periods, their use may lead to the “same object with different spectra” phenomenon. Furthermore, different crops may produce a spectral overlap, resulting in the “different objects with the same spectrum” phenomenon. Therefore, the classification accuracy is often less than ideal when classifying crops according to single-view remote sensing image data (Su et al., 2015). In response to these issues, the multiple scenes produced by continuous remote sensing image data can be used to enhance the separability of different crops, as the remote sensing images of different crops will differ at various points in a phenological period. Based on the changing spectral values of crops over time in remote sensing images, crop classification can be achieved. Jia et al. (2015) used time-series images from the HJ-1 A/B satellite as a data source to obtain the normalized difference vegetation index (NDVI) time series as a classification feature to classify crops, including spring corn, summer corn, cotton, and winter wheat. The overall classification accuracy reached 90.9%. Wang et al. (2019) used Landsat series images as data to construct the NDVI and first principal component time series reaction phenology differences. The authors also used time-weighted dynamic time planning to classify various crops, including fragrant pear, wheat, pepper, and cotton, obtaining a classification accuracy of 82.68%. Chang et al. (2017) used Gaofen 1/wide-field-view (GF-1/WFV)

---

[1] Northeast Agricultural University/ Harbin, China.

Area Editor: Fabio Henrique Rojo Baio
Received in: 10-2-2021
Accepted in: 2-15-2022

images as data to construct an NDVI time series, smoothed the time series using the harmonic analysis method, and used the decision tree (DT) and support vector machine (SVM) methods to extract the cultivated land, obtaining an overall accuracy of 92.24%.

The above-noted methods all used a single VI sequence rather than a combination of indices as a classification tool. In contrast, the present paper attempted to use a combination of multiple VIs to further improve the classification accuracy. Compared with other satellites, such as Landsat, GF-1/WFV has higher spatial resolution and a shorter revisit cycle and can construct a VI time series using a single data source. Therefore, GF-1/WFV image data were used as a remote sensing data source in this paper.

To conduct the experiment, Acheng District, Harbin City, in Heilongjiang province (China) was selected as the research area. The main crops in this area are corn and rice, while a small amount of garlic and cabbage are also grown. In this district, the phenomenon of cross-mixing between garlic and corn is common. In addition, there are a large number of built-up areas (including greenhouses) and water bodies in the study area. Owing to the large area of forest land, other vegetation, such as grass and shrubs, is primarily covered by trees. These were all classified as “other vegetation.” This paper combined four plantation indices (the NDVI, the normalized difference water index [NDWI], the enhanced VI [EVI], and the radar VI [RVI]) and used GF-1/WFV images as a data source to construct a time series of the four indices. The results of existing studies using backpropagation (BP) neural networks (Fan et al., 2017; Zhu et al., 2020), SVMs (Zhaoxin et al., 2019), and DTs (Zhou et al., 2016) to classify the main crops in the study area were compared with the classification results derived by the present study. To improve the classification accuracy of the model, the adaptive mutation particle swarm optimization (AMPSO) algorithm was used to optimize the SVM, and its effects on the classification results were analyzed.

MATERIAL AND METHODS

Acheng District, located between 126°40′–127°39′ east and 45°10′–45°50′ north, was chosen as the study area, representing a total area of 2,452 km^2. The maximum north–south distance in the study area was 84 km, the maximum east–west distance was 75 km, and the urban area was 28.85 km^2. The geographical location of the area is shown in Figure 1.

Acheng District is a mid-level mountain area with high eastern and low western terrain. It has a continental monsoon climate in the cold temperate zone, with obvious changes occurring over the four seasons. The region is prone to drought due to high temperatures and windy weather in the spring. The summer is short and hot and has a high level of precipitation. Autumn temperatures fall quickly, with frost often appearing as a result. Winters are long and very cold. The annual average temperature in the region is 3.4°C. It is hottest in July, when the average temperature is 22.7°C, with a historical maximum of 36.5°C. January is the coldest month, with an average temperature of −19.8°C and a minimum temperature of −34.2°C. The annual sunshine time is approximately 2,550 h. The accumulated temperature is 2,300°C–2,600°C, while the annual precipitation is 580–600 mm, and the number of frost-free days is 162.

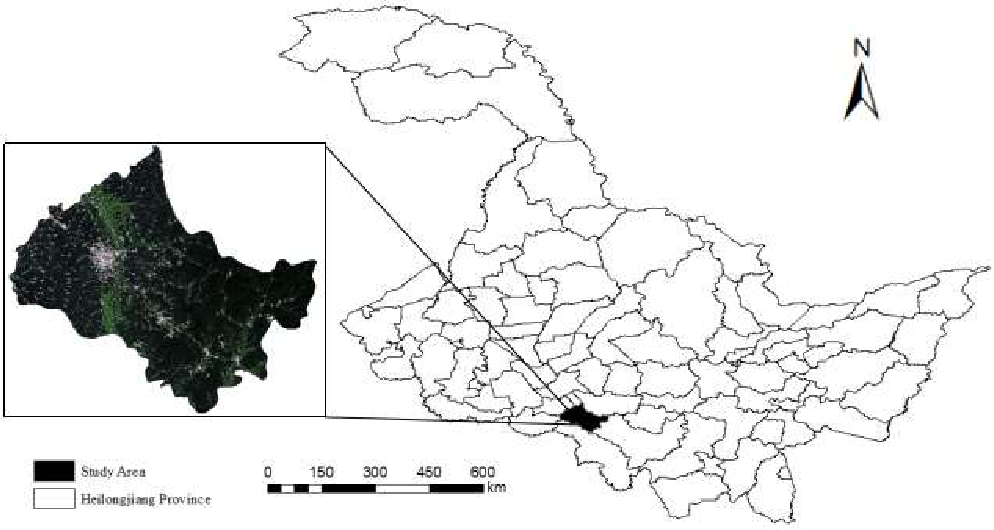

FIGURE 1. A schematic diagram of the geographical location of the study area.

In the experiment, GF-1/WFV remote sensing images were used as a data source. The WFV sensor was set to have a total of four bands, as shown in Table 1. The data were sourced from the China Resources Satellite Application Center (http://www.cresda.com/CN/). To observe the image changes throughout the crop growth period, image data from April 2018 to October 2018 were selected. The ENVI (v.5.3) software was used to perform radiometric calibration, atmospheric correction, and geometric correction on the acquired GF-1/WFV images. The software also cropped the remote sensing image data to include only the desired regions.

TABLE 1. The GF-1/WFV image band information.

Band	Description	Bandwidth/μm
B01	Blue	0.45~0.52
B02	Green	0.52~0.59
B03	Red	0.63~0.69
B04	Near Infrared	0.77~0.89

To determine the plant types and spatial distribution of the main crops in the study area, a field survey was conducted in June 2018. The coordinates (latitude and longitude) of the characteristic plots were measured, and the farming conditions and crop types of the plots were recorded. The investigation found that the ground objects in the study area mainly included water and built-up regions (including greenhouses), while the primary crops included rice, corn, garlic, cabbage, and a small number of other crops. It is noted that the garlic planting in this area begins in early April, while the harvesting occurs in early July. Cabbage is then planted in the original garlic-planting areas in middle to late July, followed by harvesting after October. Because there was spatial overlap between garlic and cabbage, the location of cabbage in August and later could be identified by garlic samples. Since the total phenological period of garlic and cabbage was roughly the same as the phenological period of corn and rice, this paper discusses garlic and cabbage as two different crops in terms of time and as a single crop in terms of space, the latter of which will be referred to as “garlic/cabbage.” According to the planting characteristics of the crops in the study area, the ground objects were divided into six types, i.e., rice, corn, garlic/cabbage, water, built-up areas, and other vegetation. A total of 1,244 sample data points were collected by the institute. The object types and the number of samples are shown in Table 2.

TABLE 2. The field sample data.

Land type	Sample quantity
Corn	360
Rice	330
Garlic/Cabbage	235
Water	75
Built-up areas	146
Other vegetations	98

The remote sensing image preprocessing was implemented using ENVI 5.3. The main processing steps included rough geometric correction, radiometric calibration, atmospheric correction, and geometric precision correction. According to the rational polynomial coefficient file included in the GF-1/WFV images, the experiment performed rough geometric correction on each original image in the time series. Then, based on the radiation calibration coefficient provided by the Resource Satellite Application Center, the digitally quantized value of each image was converted into a radiance value. The FLAASH module was also used for atmospheric correction to obtain real spectral reflectance data information. The quadratic polynomial model was used to perform geometric precision correction according to the measured data concerning the ground control points, and the precision-corrected image was then used to correct the other images. The correction error was controlled within 1 pixel to meet the image processing requirements.

Based on the crop characteristics and spectral reflectance in the research area, the NDVI, NDWI, RVI, and EVI were selected to characterize the main crops in the study area. The NDVI reflected the vegetation coverage, the RVI reflected the degree of greenness in the crops, and the EVI reflected the influence of soil background and aerosol scattering. Because rice required irrigation before transplanting, the NDWI was introduced to distinguish between the irrigated areas. According to the image spectral reflectance data after preprocessing, the four VIs were calculated as follows:

$$NDVI = \frac{\rho_{NIR} - \rho_{RED}}{\rho_{NIR} + \rho_{RED}} \tag{1}$$

$$NDWI = \frac{\rho_{GREEN} - \rho_{NIR}}{\rho_{GREEN} + \rho_{NIR}} \tag{2}$$

$$EVI = G \cdot \frac{\rho_{NIR} - \rho_{RED}}{\rho_{NIR} + 6 \cdot \rho_{RED} - 7.5 \cdot \rho_{BLUE} + 1} \tag{3}$$

$$RVI = \frac{\rho_{NIR}}{\rho_{RED}} \tag{4}$$

Where,

ρ_{NIR} is the near-infrared reflectivity;

ρ_{RED} is the red band reflectivity;

ρ_{GREEN} is the green band reflectivity;

ρ_{BLUE} is the blue band reflectivity, and

G is a gain factor.

A total of 36 scenes from nine time-series images of four plantings were indexed and merged. Among the 1,244 field-collected samples that were obtained, the sample points were randomly divided into a training set and validation set according to a ratio of 7:3, based on the number of samples from various locations. Overall, there were 870 training set samples and 374 validation set samples. A DT, BP neural network, and SVM were used for classification, while AMPSO was used to optimize the SVM. The AMPSO algorithm overcame the defects of premature convergence and made it easy to obtain a locally optimal solution. Through the mutation operation, a particle's forward direction can be changed and the local optimal point highlighted, while the global optimal solution can also be determined. The kernel parameters and penalty factors in the SVM classifier were set as particles in the AMPSO algorithm. The classification accuracy obtained after cross-validation of the training set was used as the fitness function of the AMPSO. The algorithm flow was as follows:

(1) Initialize the particle.

(2) Set the position of the particle solution as p_b and the convergence position as p_g.

(3) To judge whether to converge, if eqs (5) and (6) are satisfied, the convergence is made, and step (8) is performed. Otherwise, step (4) is performed. The equations are given as follows:

$$\sigma^2 = \sum_{i=1}^{n} \left[\frac{f_i - f_{avg}}{f}\right]^2 = 0 \tag{5}$$

$$f(p_g) \geq f_d \tag{6}$$

Where,

σ^2 is the group fitness variance;

f_i is the fitness of the *i*-th particle;

f_{avg} is the particle swarm average fitness;

f is the fitness function;

$f(p_g)$ is the global extreme, and

f_d is the theoretical extreme.

(4) The velocity and position of the particle are calculated according to eqs (7) and (8) as follows:

$$v_{id} = \omega v_{id} + c_1 r_1 (p_{id} - x_{id}) + c_2 r_2 (p_{gd} - x_{id}) \tag{7}$$

$$x_{id} = x_{id} + v_{id}. \tag{8}$$

Where,

ω is the inertia weight;

v_{id} is the particle velocity;

x_{id} is the particle position;

p_{id} is the *d*-th dimension of the individual extreme value of the *i*-th variable, and

p_{gd} is the *d*-th dimension of the global optimal solution. Furthermore, c_1 and c_2 are learning factors, and r_1 and r_2 are random numbers from 0 to 1.

(5) The population fitness variance and global extrema are calculated according to eqs (5) and (9) as follows:

$$f = \begin{cases} max\{|f_i - f_{avg}|\}, max\{|f_i - f_{avg}|\} > 1 \\ 0 \end{cases} \tag{9}$$

(6) Calculate the probability of particles mutating p_m using [eq. (10)] as follows:

$$p_m = \begin{cases} k, \sigma^2 < {\sigma_d}^2, f(p_{gd}) < f_d \\ 0 \end{cases} \tag{10}$$

Where,

k is a value within the range of [0.1, 0.4].

(7) Generate a random number *r*. If $r < p_m$, the particle is mutated, and [eq. (11)] is executed. Otherwise, execute step (3). Equation 11 is given as follows:

$$p_{gd}^k = p_{gd}^k (1 + 0.5\eta) \tag{11}$$

Where,

p_{gd}^k is the value of the *k*-th dimension of p_{gd}.

(8) Next, output p_g. The algorithm ends.

Based on the above steps, the number of iterations was set to 100. The kernel function parameter obtained when the model classification result tended to be stable was 0.135, and the penalty factor was 221.67.

The remote sensing classification accuracy evaluation generally obtains the quality of the classification result by comparing the consistency of the classified image with that of the reference image. A confusion matrix is the most commonly used accuracy evaluation method. The main accuracy evaluation parameters in the confusion matrix are the overall classification accuracy, the producer's accuracy(PA), the user's accuracy(UA), and the Kappa coefficient. The overall classification accuracy is the ratio of the number of correctly classified pixels to the total number of pixels. The producer's accuracy is the ratio of the number of pixels correctly classified as a certain type relative to the total number of pixels of that type. The user's accuracy is the ratio of the number of pixels correctly classified into a certain class to the total number of pixels classified into that class by the classifier. The Kappa coefficient is a method of measuring accuracy, based on a confusion matrix, and is calculated as follows:

$$k = \frac{P_0 - P_e}{1 - P_e}. \tag{12}$$

Where,

k is the kappa coefficient;

P_0 is the actual consistency rate, and

P_e is the theoretical consistency rate.

RESULTS AND DISCUSSION

Based on the GF-1/WFV image data, combined with the phenological characteristics of the crops in the study area, a time series curve of the four VIs was constructed, as shown in Figure 2.

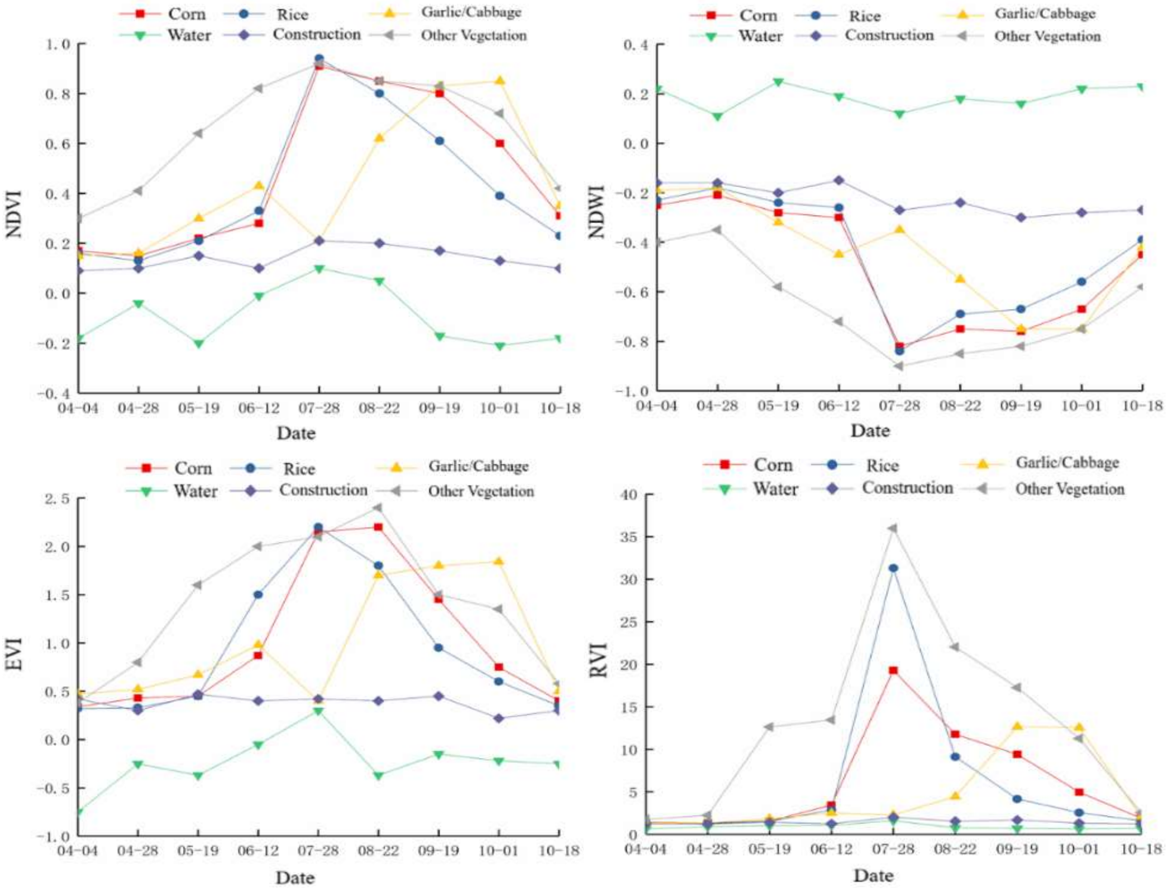

FIGURE 2. The time series curves of the vegetation indices.

Figure 2 shows that the sowing period of corn and rice extended from the end of April to mid-May; this meant that the four planting index values of the corn planting area on April 4 and 28 were close to those of bare land. As the rice fields required irrigation before the rice seedlings could be transplanted, their NDVI and EVI values decreased slightly. The sowing period of garlic was early to middle April, during which time the NDVI and EVI values of garlic were slightly higher than those of corn and rice. On May 19, both the corn and rice were in the seedling stage, and there was a slight difference in the index values among the four plantings. At this time, garlic was in the segmentation stage, meaning its NDVI and EVI values rose slowly, while its NDWI value slowly declined.

On June 12, the corn began to divide its leaves, and rice entered the tillering and jointing stage. At this time, the EVI value of rice rose significantly faster compared with corn. When the garlic entered the period of garlic stalk elongation and bulb expansion, the NDVI value also began to increase, while the NDWI value began to decrease, representing behavior significantly different from that observed in the time series curves of rice and corn. On July 28, corn was in the tasseling and silking period, and rice was in the heading period. The NDVI, EVI, and RVI values of the two crops increased rapidly, while their NDWI values decreased rapidly. Since garlic was harvested in early July, and cabbage was harvested in middle to late July, the NDVI, EVI, and RVI values of the corresponding areas on July 28 were significantly lower than those of corn and rice, while the NDWI values of these areas were higher.

On August 22, when the rice was in the poplar flower filling stage, its NDVI, EVI, and RVI values began to fall, while its NDWI value began to rise. When corn reached the filling stage, the trends of its four cropping indices were roughly the same as those of rice, but the rate of decline was significantly slower than that of rice. At this time, cabbage was in the growth and development stage, and its VI was on the rise, although its NDVI and RVI values were significantly lower than those of corn and rice.

On September 19, both the corn and rice were in the maturity stage. The NDVI and EVI values of the corn were significantly higher than those of rice, while the EVI and RVI values of cabbage were significantly higher than those of both corn and rice. The NDVI and EVI values of cabbage reached a maximum on October 1, at which point they were significantly higher than those of the other crops, while the VI values of the other crops exhibited a rapid decline during this period.

On October 18, several crops were harvested, and the VI values exhibited little difference. In addition, several other non-crop areas differed significantly concerning the presence of water bodies and vegetation, while the overall trend of the time series curve regarding construction land remained stable throughout the entire phenological period. Other vegetation mainly included forest areas, grasslands, and other crops in small areas. Among them, the distribution of forest areas was relatively concentrated. Except for during the peak period of crop growth, the VI values of the forests were higher than those of the crops.

Next, the training sample set and fused image were input into the DT classifier, the BP neural network, the SVM classifier, and the AMPSO–SVM classifier. The crops in the study area were classified according to the four indices. The spatial distribution of the ground objects in the study area is shown in Figure 3.

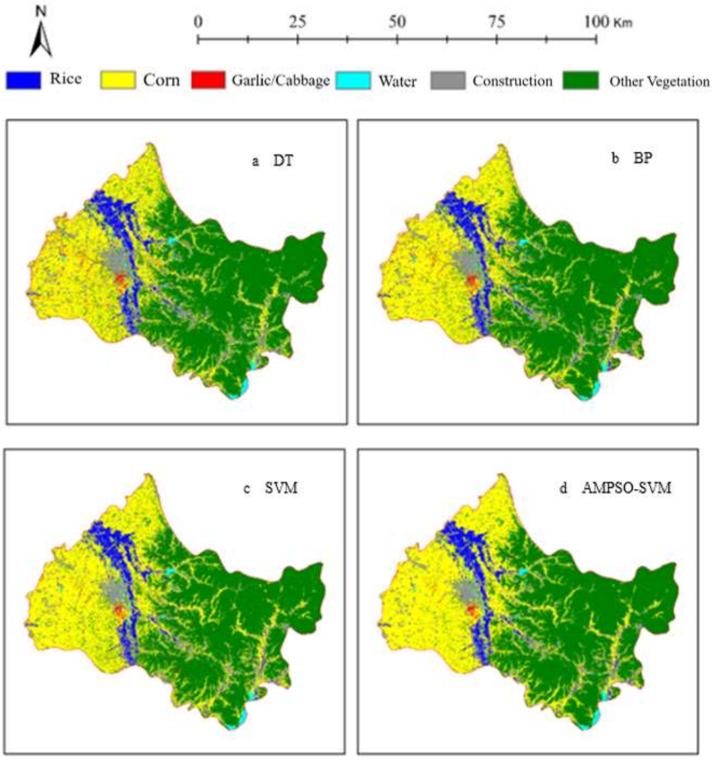

FIGURE 3. The classification results graph.

Figure 3 shows that the eastern part of Acheng District is a mountainous area that is primarily covered by forest land. Only a small amount of arable land has been developed in this area (by the sides of roads), and only corn can be grown owing to water sources and topographical restrictions. Thus, corn is scattered throughout this area. Crop planting areas are mainly concentrated in the western plains and the surrounding urban areas. Rice planting occurs mostly on both banks of the Ash River, and most of these areas are adjacent to corn, as indicated by the blue belt-shaped area in Figure 3. Garlic/cabbage planting is mostly concentrated southeast of the city center, although a small amount is mixed with corn in other areas. The most abundant crop is corn, which is also mixed with a small amount of other vegetation. Among the crops, rice had the best overall classification effect, with only a small amount being mistakenly classified as corn or other vegetation. The garlic/cabbage area was mistakenly classified as corn, which may have been caused by mixing with corn. When garlic and corn are planted next to each other, some occlusion on the boundary of the two will be present, resulting in mixed pixels. This may cause misclassification, although other large-scale garlic areas will not be affected. A small amount was misclassified into construction land, likely because the cabbage was not harvested in time after the garlic was harvested in early July, resulting in a VI value close to that of bare land. At the same time, it was affected by the buildings in the image, causing a small area to be misclassified. Corn had the largest planting area and was mixed with other vegetation. Therefore, it was often mistakenly classified as garlic/cabbage or other vegetation.

In this research, 374 sample points collected in the field were used to verify the accuracy of the classification results of the four classifiers. Among them, the verification sample sites included 108 corn sites, 99 rice sites, 71 garlic/cabbage sites, 23 water sites, 44 built-up sites, and 29 other sites. The calculated accuracy comparison results are shown in Table 3.

TABLE 3. A comparison of the classification accuracy.

Land cover and crop types	DT		BP		SVM		AMPSO-SVM	
	PA/%	UA/%	PA/%	UA/%	PA/%	UA/%	PA/%	UA/%
Corn	88.89	93.20	87.96	94.06	88.89	88.89	93.52	92.66
Rice	90.91	92.78	88.89	94.62	91.92	96.81	95.96	98.96
Garlic/Cabbage	88.73	86.30	91.55	91.55	85.92	96.83	91.55	94.20
Water	95.65	100.00	95.65	100.00	95.63	100.00	95.65	100.00
Built-up areas	93.18	85.42	95.45	84.00	100.00	86.27	100.00	91.67
Other vegetation	72.41	67.74	80.76	64.86	89.66	72.22	89.66	86.67
OA/ %	89.04		89.84		90.91		94.39	
Kappa coefficient	0.8612		0.8719		0.8851		0.9287	

As shown in Table 3, the classification results of the four methods were satisfactory, with the overall classification accuracy being above 89%. Among the methods, the SVM classifier had the best classification effect, with an overall accuracy of 90.91% and a Kappa coefficient of 0.8851. The BP classifier was second, with an overall accuracy of 89.84% and a Kappa coefficient of 0.8719. The overall accuracy of the DT classifier was 89.04%, and its Kappa coefficient was 0.8612.

The DT classification method made full use of the spectral differences among various crops. It could realize the effective mining of spectral information and combined the VI at each stage of the growth period. Following hierarchical extraction, it can also improve the classification accuracy to give it high accuracy. A BP neural network essentially realizes a mapping function from the input to output stages. It can automatically extract "reasonable rules" between input and output data through learning, making the accuracy of the BP network classification higher than that of DT. The SVM classifier performed the best among the three classification methods and was subsequently optimized in terms of hyperparameter selection using the AMPSO algorithm. It was determined that the AMPSO–SVM classifier had the best classification effect when the kernel parameter was 0.135 and the penalty factor was 221.67. In this case, it achieved an overall classification accuracy of 94.39% and a Kappa coefficient of 0.9287. Compared with the unmodified SVM classifier, the overall classification accuracy of the optimized classifier was increased by 3.48%, and the Kappa coefficient was increased by 0.0436.

CONCLUSIONS

Multi-view GF-1/WFV remote sensing images were used as data sources to construct a time series for the NDVI, NDWI, EVI, and RVI plantation indices covering the complete growth period of crops in Acheng District, Harbin City, Heilongjiang province, in China. Combining this with the collected sample field data, a DT, BP neural network, SVM, and AMPSO–SVM were used to classify the main crops in the research area. The results revealed the following.

(1) The four VIs that were calculated, based on GF-1/WFV remote sensing images, were able to describe the growth status of different crops in the study area at different periods. The combination of the time series of the four VIs was able to accurately express the dynamic change process of various areas and effectively identified the main crops in the study area.

(2) The DT, BP neural network, and SVM classifiers all achieved high classification accuracy. The overall accuracy reached above 89%, indicating that the combination of the four planting index time series obtained, based on GF-1/WFV remote sensing images, could be used as the classification feature of a classifier to achieve high-precision crop classification. The SVM classifier had the highest classification accuracy, reaching 90.91% and a Kappa coefficient of 0.8851, indicating it as being the most effective in large-area remote sensing image classification.

(3) The classification effect of the SVM was significantly improved after optimization with the AMPSO algorithm. The classification effect was best when the kernel parameter was set as 0.135 and the penalty factor was 221.67. In this case, the overall classification accuracy reached 94.39%, and the Kappa coefficient was 0.9287. Compared with the SVM classifier, the classification accuracy was increased by 3.48%, while the Kappa coefficient was increased by 0.0436.

ACKNOWLEDGMENTS

This study is supported by the reform and development funds of local universities supported by the central government of Heilongjiang provincial undergraduate universities (high-level talent programs, 2020GSP15).

REFERENCES

Caiyun Z, Zhixiao X (2012) Combining object-based texture measures with a neural network for vegetation mapping in the everglades from hyperspectral imagery. Remote Sensing of Environment 124(9): 310-320. DOI: https://doi.org/10.1016/j.res.2012.05.015

Chang BH, Wang J T, Luo Y L, Wang Y H, Wang Y M (2017) Cultivated land extraction based on gf-1/wfv remote sensing in shenwu irrigation area of hetao irrigation district. Transactions of the Chinese Society of Agricultural Engineering 33(23):188-195. DOI: https://doi.org/10.11975/j.issn.1002-6819.2017.23.024

Chang-an L, Zhong-xin C, Yun S, Jin-song C, Hasi T, Pan HZ (2019) Research advances of sar remote sensing for agriculture applications: a review. Journal of Integrative Agriculture 18(003): 506-525. DOI: https://doi.org/10.1016/S2095-3119(18)62016-7

Fan YY, Qian YR, Liu Y, Huang Z, Software SO, University X (2017) Cotton recognition method for remote sensing image based on bp neural network. Computer Engineering and Design 38(05): 1356-1360. DOI: https://doi.org/10.16208/j.issn1000-7024.2017.05.044

Han Y, Meng J (2019) A review of per-field crop classification using remote sensing. Remote Sensing for Land & Resources 31(02): 1-9. DOI: https://doi.org/10.6046/gtzyyg.2019.02.01

Liu Jia, Wang Limin, Yang Fugang, Yang Lingbo, Wang Xiaolong (2015) Remote sensing estimation of crop planting area based on HJ time-series images 31(3):199-206. DOI: https://doi.org/10.3969/j.issn.1002-6819.2015.03.026

Qian S, Hu Q, Zhou Q, Ciara H, Xiang M, Tang H (2017) In-season crop mapping with gf-1/wfv data by combining object-based image analysis and random forest. Remote Sensing 9(11):1184. DOI: https://doi.org/10.3390/rs9111184

Qing-bo Zhou, Qiang-yi YU, Jia LIU, Wen-bin WU, Hua-jun Tang (2017) Perspective of chinese gf-1 high-resolution satellite data in agricultural remote sensing monitoring. Journal of Integrative Agriculture16(02):242-251. DOI: https://doi.org/10.1016/S2095-3119(16)61479-X

Silva AF, Paula BA, Zimback C, Landim P (2013) Geostatistics and remote sensing methods in the classification of images of areas cultivated with citrus. Engenharia Agrícola 33(6):1245-1256. DOI: https://doi.org/10.1590/S0100-69162013000600017

Su W, Jiang F, Zhu D, Zhan J, Zhang X (2015) Extraction of maize planting area based on decision tree and mixed-pixel unmixing methods. Nongye Jixie Xuebao/Transactions of the Chinese Society of Agricultural Machinery 46(9): 289-295, 301. DOI: https://doi.org/10.6041/j.issn.1000-1298.2015.09.042

Wang X, Qiu P, Y Li, Mingxing C, University, F, Amp N (2019) Crops identification in Kaikong River Basin of Xinjiang based on time series Landsat remote sensing images. Journal of Agricultural engineering 35(16):180-188. DOI: https://doi.org/10.11975/j.issn.1002-6819.2019.16.020

Yinjiang J, Tao J, Zhongbin S,Qingming K, Xiaoyu Z, Yubo S (2020) Research on typical crop classification method based on improved SVM algorithm. Journal of Northeast Agricultural University (7):77-85. DOI: https://doi.org/10.19720/j.cnki.issn.1005-369.2020.07.0010

Zhaoxin HE, Zhang M, Bingfang WU, Xing Q (2019) Extraction of summer crop in jiangsu based on google earth engine. Journal of Geo-Information Science 21(05):752-766. DOI: https://doi.org/10.12082/dqxxkx.2019.180420

Zhou J, Li C, Shi L, Shi S, Huai H (2016) Crops distribution information extracted by remote sensing based on decision tree and object-oriented method. Transactions of the Chinese Society for Agricultural Machinery 47(09):318-326+333. DOI: https://doi.org/10.6041/j.issn.1000-1298.2016.09.043

Zhu L, Zhang S, Xu S, Zhao H, Chen S, Wei D (2020) Classification of uav-to-ground targets based on micro-doppler fractal features using ieemd and ga-bp neural network. IEEE Sensors Journal 20(1). DOI: https://doi.org/10.1109/JSEN.2019.2942081